A chemically stabilized sulfur cathode for lean electrolyte lithium sulfur batteries

Chao Luo[a,b], Enyuan Hu[c], Karen J. Gaskell[d], Xiulin Fan[a], Tao Gao[e], Chunyu Cui[a], Sanjit Ghose[f], Xiao-Qing Yang[c], and Chunsheng Wang[a,d,1]

[a]Department of Chemical and Biomolecular Engineering, University of Maryland, College Park, MD 20742; [b]Department of Chemistry and Biochemistry, George Mason University, Fairfax, VA 22030; [c]Chemistry Division, Brookhaven National Laboratory, Upton, NY 11973; [d]Department of Chemistry and Biochemistry, University of Maryland, College Park, MD 20742; [e]Department of Chemical Engineering, Massachusetts Institute of Technology, Cambridge, MA 02139; and [f]National Synchrotron Light Source II, Brookhaven National Laboratory, Upton, NY 11973

Edited by Thomas E. Mallouk, The Pennsylvania State University, University Park, PA, and approved May 15, 2020 (received for review April 3, 2020)

Lithium sulfur batteries (LSBs) are promising next-generation rechargeable batteries due to the high gravimetric energy, low cost, abundance, nontoxicity, and high sustainability of sulfur. However, the dissolution of high-order polysulfide in electrolytes and low Coulombic efficiency of Li anode require excess electrolytes and Li metal, which significantly reduce the energy density of LSBs. Quasi-solid-state LSBs, where sulfur is encapsulated in the micropores of carbon matrix and sealed by solid electrolyte interphase, can operate under lean electrolyte conditions, but a low sulfur loading in carbon matrix (<40 wt %) and low sulfur unitization (<70%) still limit the energy density in a cell level. Here, we significantly increase the sulfur loading in carbon to 60 wt % and sulfur utilization to ∼87% by dispersing sulfur in an oxygen-rich dense carbon host at a molecular level through strong chemical interactions of C–S and O–S. In an all-fluorinated organic lean electrolyte, the C/S cathode experiences a solid-state lithiation/delithiation reaction after the formation of solid electrolyte interphase in the first deep lithiation, completely avoiding the shuttle reaction. The chemically stabilized C/S composite retains a high reversible capacity of 541 mAh·g^{-1} (based on the total weight of the C/S composite) for 200 cycles under lean electrolyte conditions, corresponding to a high energy density of 974 Wh·kg^{-1}. The superior electrochemical performance of the chemical bonding-stabilized C/S composite renders it a promising cathode material for high-energy and long-cycle-life LSBs.

lithium sulfur batteries | lean electrolyte | chemical bonding | carbon | oxygen

Lithium ion batteries (LIBs) are the dominant energy storage devices for portable electronics and electric vehicles. However, the use of toxic and expensive cobalt-based cathode materials not only limits the energy density of LIBs due to the low capacity (<200 mAh·g^{-1}) of $LiCoO_2$ and $LiNi_{1/3}Mn_{1/3}Co_{1/3}O_2$ cathodes but also triggers severe environment and sustainability challenges (1–3). To date, considerable research efforts have been devoted to developing low-cobalt-content cathode materials such as layered $LiNi_{0.8}Mn_{0.1}Co_{0.1}O_2$ with a capacity of ∼200 mAh·g^{-1} or cobalt-free olivine-structured $LiFePO_4$ with a capacity of ∼170 mAh·g^{-1} (4–9). Although great success has been achieved for these cathode materials, the capacity is still much lower than that of a commercial anode such as graphite (372 mAh·g^{-1}) (10, 11). Therefore, the bottleneck of high-energy LIBs is a lack of a high-energy cathode to couple with the high-capacity anode.

Sulfur cathode has a theoretical capacity of 1672 mAh·g^{-1} (12–19). The high energy density (∼2,600 Wh·kg^{-1}) of lithium sulfur batteries (LSBs) has attracted extensive research interest due to the low cost, nontoxicity, abundance, and high sustainability of sulfur (20–24). However, the sulfur cathode suffers from two major challenges (25–30). First, the dissolution of high-order polysulfide intermediates (Li_2S_8-Li_2S_4) in the organic electrolytes causes severe sulfur loss in the cathode, reducing the cycle life of LSBs. The dissolution of high-order polysulfide intermediates also requires flooded electrolyte (FE) to achieve a high-power density, sacrificing the total energy density. Second, the low cycling Coulombic efficiency (CE) of Li plating/stripping of <99.2% continuously consumes Li anode and electrolytes during cycling, requiring excess Li and electrolytes, thus further reducing the energy density of LSBs. To circumvent these challenges, a myriad of conductive carbon materials such as graphene, carbon nanotube, porous carbon, and expanded graphite have been used to prevent the dissolution of polysulfides and increase the electrical conductivity of sulfur cathode (31–36). However, a high capacity of >800 mAh g^{-1} for hundreds of cycles in Li–S batteries can only be achieved in FE with excess Li, because of the low cycling CE of Li plating/stripping and the dissolution of polysulfides in the liquid electrolyte. The use of FE and excess Li reduces the energy density, impeding the large-scale application of LSBs. In addition, excess electrolyte with dissolved polysulfides also promotes the shuttle reaction, accelerating the capacity decay. To fulfill the high energy and long cycle life LSBs, the ratio of electrolyte to sulfur should be minimized to <5 mL_E/g_S, and Li plating/stripping CE should be maximized to a high value of >99.2%.

Electrolyte additives, polymer gel, and porous carbon composite reservoirs have been used to minimize the electrolyte consumption in LSBs (37–40), at a price of reducing the electrochemical performance. To achieve high-performance LSBs under lean electrolyte conditions (LEC), the electronic insulating sulfur should be dispersed in a conductive carbon matrix

Significance

Sulfur is a promising cathode material for rechargeable lithium batteries due to its high capacity, low cost, abundance, and high sustainability. However, lithium sulfur batteries suffer from poor cycle life and low energy density under lean electrolyte conditions because of the dissolution of lithium polysulfide intermediates. Here, we report that the chemical bonding between sulfur and carbon/oxygen in an oxygen-rich dense carbon host can stabilize sulfur and improve the stability of lean electrolyte lithium sulfur batteries. This work opens up a way to develop chemical bonding-stabilized sulfur materials for stable and high-energy lithium sulfur batteries.

Author contributions: C.L., and C.W. designed research; C.L., E.H., K.J.G., C.C., and S.G. performed research; C.L. and X.F. contributed new reagents/analytic tools; C.L., E.H., K.J.G., T.G., S.G., and X.-Q.Y. analyzed data; and C.L., E.H., and C.W. wrote the paper.

The authors declare no competing interest.

This article is a PNAS Direct Submission.

[1]To whom correspondence may be addressed. Email: cswang@umd.edu.

This article contains supporting information online at https://www.pnas.org/lookup/suppl/doi:10.1073/pnas.2006301117/-/DCSupplemental.

CHEMISTRY

at a molecular level and react with lithium through a solid-state reaction without the involvement of liquid electrolytes. By carbonizing organic/polymer materials and sulfur at a high temperature of 600 °C, S_8 can be decomposed into S_2 and S_3 and bonded to C and other elements in the carbon matrix, forming a molecular-level dense S/C composite. The small sulfur molecules ($S_{2–3}$) in C/S composite could react with Li-ions to generate insoluble Li_2S_2 and Li_2S through a solid-state reaction. Yin and Franco (41) used a continuum modeling method to prove that the final discharge product of LSBs based on ultramicroporous carbons is a mixture of Li_2S and Li_2S_2, the resistivity of which plays a critical role in battery capacity. Lowering the resistivity of the final product enhances the sulfur utilization, resulting in a higher discharge capacity. Therefore, forming a molecular-level dense S/C composite improves the capacity and energy density of LSBs.

Small-sulfur/carbon composites (SSCCs) synthesized by carbonizing sulfur and organic/polymer materials exhibited long cycle life and high rate capability in LSBs (42–44). However, Li/SSCCs batteries still suffer from two challenges: 1) The low sulfur content (<40 wt %) and low sulfur utilization (<70%) lowers the overall energy density of the sulfur cathode and 2) the low CE of Li plating/stripping consumes electrolytes and Li metal, further lowering the energy density. To increase the sulfur content and the sulfur utilization, we use an oxygen-rich organic material (perylenetetracarboxylic dianhydride, PTCDA) and a nitrogen-rich polymer (polyacrylonitrile, PAN) as carbon precursors to prepare SSCCs, in which the sulfur content can be increased to a recorded 60 wt %. The high sulfur loading in molecular level distribution is attributed to the increased oxygen content (~8 wt %) in the carbonized PTCDA–PAN matrix, which stabilizes sulfur by S–O bond. In addition, the nitrogen doping in the carbon promotes the bond formation between sulfur and oxygen, further increasing the sulfur content and immobilization in the carbon composite (45–47). The molecular level distribution of sulfur in the carbon matrix increases the sulfur utilization to ~87% during lithiation/delithiation. Moreover, the nonflammable all-fluorinated organic electrolyte (1.0 M $LiPF_6$ in fluoroethylene carbonate/3,3,3-fluoroethylmethyl carbonate/1,1,2,2-tetrafluoroethyl-2′,2′,2′-trifluoroethyl ether [FEC:FEMC:HFE, 2:6:2 by weight]) enhances the CE of lithium metal anode to 99.2% by forming LiF-rich solid electrolyte interphase (SEI) to suppress the lithium dendrite growth (48). The synergy of the high sulfur content SSCCs and all-fluorinated organic electrolytes enables high-energy and stable LSBs under LEC.

Results

Three types of SSCCs were synthesized by annealing the mixture of carbon precursors (oxygen-rich PTCDA and nitrogen-rich PAN) and sulfur in a sealed vacuum glass tube. The oxygen-rich PTCDA and nitrogen-rich PAN are used as carbon precursors to introduce oxygen and nitrogen into the SSCCs to produce the carbonized PTCDA–PAN–S, which is denoted as CPAPN–S composite. The oxygen in PTCDA forms chemical bonding with small sulfur molecules, while nitrogen in PAN stabilizes sulfur through lithium ions after first lithiation, all of which enhance the sulfur content and utilization in the CPAPN–S composite. As controls, CPTCDA–S and CPAN–S composites were synthesized by using only PTCDA or PAN as carbon precursors, separately. The CPTCDA–S, CPAN–S, CPAPN–S, and the three types of carbons (CPTCDA, CPAN, and CPAPN) without sulfur were characterized by X-ray diffraction (XRD), Raman spectroscopy, Fourier-transform infrared spectroscopy (FTIR), X-ray photoelectron spectroscopy (XPS), scanning electron microscope (SEM), and transmission electron microscopy (TEM). As indicated in *SI Appendix*, Fig. S1 *A–C*, three types of carbons (CPTCDA, CPAN, and CPAPN) exhibit amorphous structures. After cocarbonization with sulfur, CPAPN–S (Fig. 1*A*) and CPAN–S (*SI Appendix*, Fig. S1*E*) are still in amorphous structure due to the good confinement of CPAPN and CPAN to sulfur, while CPTCDA–S (*SI Appendix*, Fig. S1*D*) shows the crystal structure of sulfur, demonstrating that CPTCDA is not able to confine all of the sulfur, and there are still some ring-structured S_8 in CPTCDA–S. Raman and FTIR spectroscopy were used to further analyze the structure of CPTCDA–S, CPAN–S, CPAPN–S, and the three types of carbons. The strong Raman peaks (*SI Appendix*, Fig. S2 *A–C*) at 1,350 cm^{-1} and 1,580 cm^{-1} represent the D band (disordered carbon) and G band (graphitic carbon) of the carbonized PTCDA, PAN, and PTCDA/PAN. In CPAPN–S (Fig. 1*B*) and CPTCDA–S (*SI Appendix*, Fig. S2*D*), there are two sharp peaks at 475 cm^{-1} and 930 cm^{-1} and one small peak at 790 cm^{-1}, representing S–S stretching mode, C–O vibration, and C–S stretching mode, respectively (49, 50). The two broad peaks at 310 cm^{-1} and 370 cm^{-1}

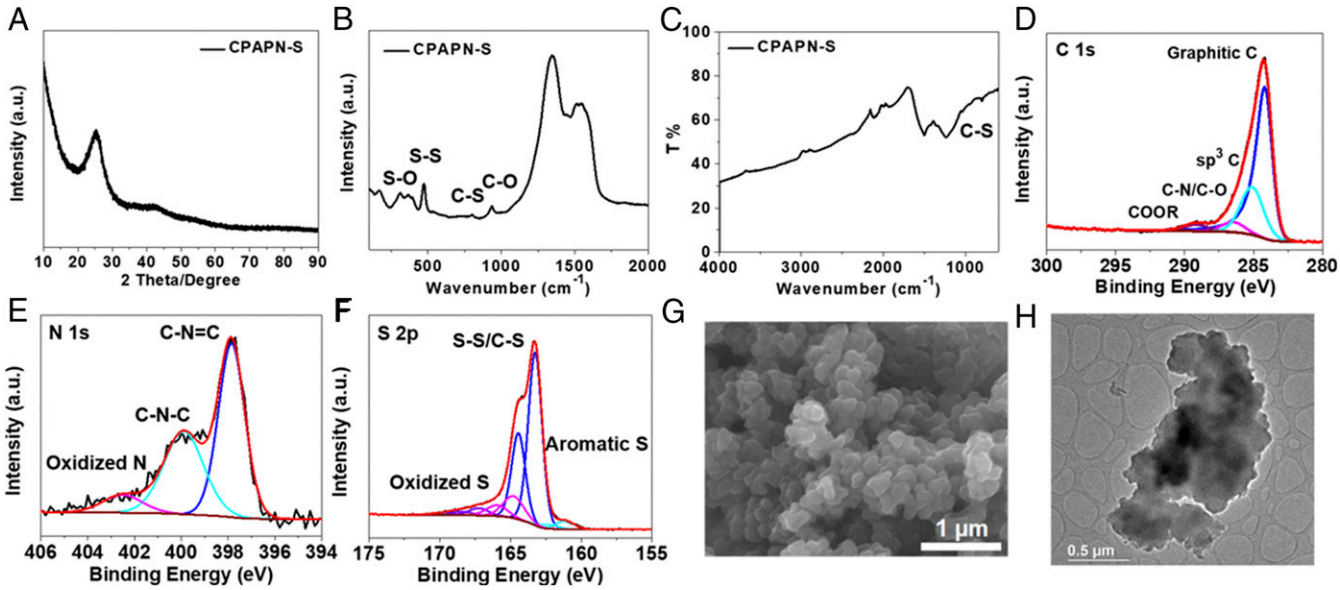

Fig. 1. Material characterizations for CPAPN–S. (*A*) XRD pattern. (*B*) Raman spectrum. (*C*) FTIR spectrum. (*D–F*) XPS spectra for (*D*) C 1s, (*E*) N 1s, and (*F*) S 2p. (*G*) SEM image. (*H*) TEM image.

stand for the S–O vibrations (50). In FTIR spectra for CPTCDA, CPAN, CPAPN, CPTCDA–S, and CPAN–S (*SI Appendix*, Fig. S3) and CPAPN–S (Fig. 1*C*), the two strong peaks at 1,240 cm^{-1} and 1,510 cm^{-1} stand for the alicyclic chain vibrations and aromatic ring chain vibrations, respectively, while the small peak at ~790 cm^{-1} (Fig. 1*C*) represents C–S vibration in CPAPN–S. The surface structure of CPAPN–S was further characterized by XPS in Fig. 1 *D*–*F*, where the C 1s peak at 284.2 eV (Fig. 1*D*) corresponding to graphitic carbon is used as a reference binding energy. The peak has been fit to show the binding energies of the different functionalities of carbon. The N 1s spectrum in Fig. 1*E* demonstrates that there are three types of nitrogen bondings in the CPAPN–S composite, which are assigned to pyridinic nitrogen at 397.8 eV, pyrrolic nitrogen at 399.9 eV, and oxidized nitrogen at 402.5 eV (51). The pyridinic and pyrrolic nitrogens come from the carbonized PAN, while the oxidized nitrogen is the product of the reaction between nitrogen in the carbonized PAN and oxygen in the carbonized PTCDA. The S 2p spectrum in Fig. 1*F* shows that there are four types of sulfur in the CPAPN–S composite, which are assigned to aromatic sulfur at 161.1/162.3 eV, sulfur in S–S and S–C groups at 163.2/164.4 eV, sulfur in S-O-C group at 164.8/166.0 eV, and the other oxidized sulfur at 167.2/168.4 eV and 169.3/170.4 eV (52). The in situ infiltration of small sulfur molecules in the carbonized PTCDA and PAN generates a variety of C–S and O–S bondings in the CPAPN–S composite, which could enhance the sulfur content and stabilize the small sulfur molecules in the composite. The morphology of the SSCCs and the corresponding carbons is characterized by SEM. As shown in Fig. 1*G* and *SI Appendix*, Fig. S4, the carbonized PTCDA, PAN, and the mixture of PTCDA and PAN consist of microsized particles, while the particles of SSCCs decrease to nanoscale due to the reaction between sulfur and organic/polymer-derived carbons. TEM and elemental mappings were performed to further characterize CPAPN–S composite. As shown in Fig. 1*H* and *SI Appendix*, Fig. S5, nanosized CPAPN–S particles aggregate into a microsized particle, and the oxygen, nitrogen, and sulfur are uniformly distributed in the carbon matrix and are bonded to each other, which strongly stabilizes sulfur. As demonstrated by the thermogravimetric (TG) analysis in *SI Appendix*, Fig. S6, only 4% weight loss of CPAPN–S composite was observed after annealing to 600 °C, while the elemental analysis result shows that there is 60 wt % of sulfur, 28 wt % of carbon, 2 wt % of nitrogen, and 8 wt % of oxygen in the composite. The content of sulfur in CPAPN–S is also confirmed by the TEM elemental analysis in *SI Appendix*, Fig. S7. The chemical bonding between sulfur and oxygen/carbon stabilizes the small sulfur molecules and prevents the sulfur evaporation. The material characterizations prove the chemical bonding of S–O and S–C in the CPAPN–S composite.

The electrochemical performance of the SSCCs were first evaluated in coin cells with areal C/S loading of ~1.2 mg/cm^2 in the flooded commercial carbonate electrolyte (1M $LiPF_6$-EC/DMC). To activate the bonded sulfur in the SSCCs composite, the SSCC cathodes were discharged to a low potential of 0.5 V at a low current density of 50 $mA{\cdot}g^{-1}$ in the first few cycles to ensure that all of the bonded sulfur in the SSCCs was fully lithiated. In the first discharge (*SI Appendix*, Fig. S8*A*), CPTCDA–S shows a small plateau at 2.4 V, corresponding to the formation of high-order polysulfides from ring-structured S_8 (*SI Appendix*, Fig. S1*D*). The polysulfides can react with the carbonate electrolyte, so they are disappeared in the second cycle. This phenomenon further demonstrates that CPTCDA is not able to confine all of the sulfur as small sulfur molecules, which is also indicated by the XRD result in *SI Appendix*, Fig. S1*D*. Although a high delithiation capacity of 945 $mAh{\cdot}g^{-1}$ is achieved for CPTCDA–S cathodes in the first cycle, the capacity quickly drops to 370 $mAh{\cdot}g^{-1}$ after 60 cycles with a low CE of ~95% (*SI Appendix*, Fig. S8*B*). The fast capacity fading confirms that CPTCDA cannot confine the large amount of sulfur and prevent the shuttle effect. Unlike CPTCDA–S, the CPAN–S and CPAPN–S do not have crystallized S_8 (*SI Appendix*, Fig. S1*E* and Fig. 1*A*) and do not form high-order polysulfides in the first cycle, but only show sloping discharge plateaus centered at 1.0 V (*SI Appendix*, Fig. S8*C*) and 0.8 V (*SI Appendix*, Fig. S8*E*), respectively. The irreversible plateau of CPAPN–S at 0.8 V in the first lithiation is to activate chemically bonded S by generating Li_2O and SEI on the C/S surface. In the second cycle, the discharge plateaus of both CPAN–S and CPAPN–S increase to 1.8 V, demonstrating that there is a large overpotential in the first discharge to overcome the chemical bonding between sulfur and oxygen/carbon in the composites. CPAN–S delivers a high reversible capacity of 590 $mAh{\cdot}g^{-1}$ based on the total weight of CPAN–S for 50 cycles in the cutoff window from 0.5 V to 3 V (*SI Appendix*, Fig. S8*D*). After fully activation and narrowing the cutoff window (1 to 3 V), CPAN–S still delivers a reversible capacity of ~450 $mAh{\cdot}g^{-1}$, which is much more stable than that of CPTCDA–S. When PAN is partially replaced by PTCDA, the introduction of oxygen in CPAPN–S further enhances the reversible capacity to ~870 $mAh{\cdot}g^{-1}$ for 50 cycles based on the total weight of CPAPN–S (*SI Appendix*, Fig. S8*F*), corresponding to 87% sulfur utilization. The reversible capacity of CPAPN–S is

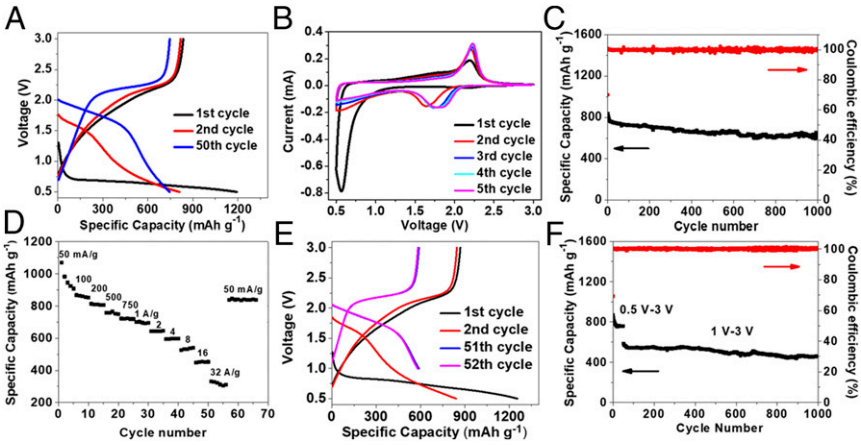

Fig. 2. Electrochemical behaviors of CPAPN–S. (*A*) The galvanostatic charge and discharge curves at 500 $mA{\cdot}g^{-1}$. (*B*) CV at 0.1 $mV{\cdot}s^{-1}$. (*C*) Delithiation capacity and CE versus cycle number at 500 $mA{\cdot}g^{-1}$. (*D*) Rate performance at various current densities. (*E*) The galvanostatic charge and discharge curves at different cutoff windows at 500 $mA{\cdot}g^{-1}$. (*F*) Delithiation capacity and CE versus cycle number at different cutoff windows at 500 $mA{\cdot}g^{-1}$. (Note: the specific capacity is calculated based on the total weight of C/S composite with an area mass loading of 1.2 $mg{\cdot}cm^{-2}$.)

mainly contributed by sulfur, because the capacity of CPAPN is only ~90 mAh·g^{-1} after 50 cycles (*SI Appendix*, Fig. S9). Even though narrowing the cutoff window (1 to 3 V), CPAPN–S still retains a reversible capacity of 625 mAh·g^{-1} after 100 cycles (*SI Appendix*, Fig. S8*F*), corresponding to an energy density of 1,125 Wh·kg^{-1}. The high capacity and good cyclic stability of CPAPN–S render it a promising cathode material for high energy LSBs. Therefore, CPAPN–S was selected for further detailed characterization and analysis.

The electrochemical performance of CPAPN–S at a high current rate of 500 mA·g^{-1} is shown in Fig. 2*A*. The potential of initial discharge plateau, which is 0.8 V at 50 mA·g^{-1} (*SI Appendix*, Fig. S8*E*), is further decreased to 0.6 V due to the larger overpotential at a high current density. In the following cycles, the discharge plateau gradually increases back to 1.8 V, corresponding to the lithiation of small sulfur molecules. Coincident with the charge/discharge behaviors, the cyclic voltammograms (CV; Fig. 2*B*) also show a sharp peak at 0.6 V in the first cathodic scan, while the cathodic peak shifts to a higher value, and a pair of redox peaks at 1.8 V/2.2 V appear in the following scans. The large overpotential in the first discharge demonstrates that there is an activation process for the CPAPN–S to release more sulfur confined by the chemical bonding for the redox reaction. In the long-term cycling test (Fig. 2*C*), CPAPN–S delivers an initial capacity of 836 mAh·g^{-1} with an initial CE of 70.1% and retains a reversible capacity of 626 mAh·g^{-1} and high CE of ~100% after 1,000 cycles, corresponding to a very slow capacity decay rate of 0.025% per cycle. The low CE in the first cycle is due to the activation of bonded S by forming Li-O and the growth of SEI layer, while the CE of CPAPN–S quickly increases to close to 100% after a few cycles. To mitigate the huge consumption of Li in the first cycle caused by the low initial CE, the CPAPN–S composite can be chemically prelithiated during the material synthesis process by adding a small amount of Li metal (or Li_2S) in the PTCDA–PAN–S mixture for the carbonization. To further improve the initial CE of this type of LSBs, there are two approaches: 1) using the artificial SEI consisting of LiF to protect the lithium metal anode and sulfur cathode, mitigating the consumption of lithium ions and electrolytes by SEI formation in the first cycle (53), or 2) optimizing the electrolyte and substrate to achieve the lithiophobic SEI and lithiophilic substrate for lithium metal anode, which improve the Li plating/stripping CE and alleviate the Li dendrite growth (54). Since S is distributed in the carbon matrix at a molecule level, CPAPN–S has very high rate capability. Fig. 2*D* shows the rate performance of CPAPN–S at various current densities from 50 mA·g^{-1} to 32 A·g^{-1}. A reversible capacity of 322 mAh·g^{-1} can be retained even at an ultrahigh current density of 32 A·g^{-1}. When the current density is decreased back to 50 mA·g^{-1}, a reversible capacity of 840 mAh·g^{-1} can still be retained, demonstrating the robust reaction kinetics of CPAPN–S. As shown in Fig. 2*A*, after full activation (50 cycles), the capacity of CPAPN–S cathodes below 1.5 V is very small, so the lower cutoff potential limit increases from 0.5 V to 1 V (Fig. 2*E*); similar charge/discharge behaviors to that in Fig. 2*A* are achieved, demonstrating that the cutoff window change does not impact the electrochemical performance of CPAPN–S, while the reversible capacity of CPAPN–S is decreased to 588 mAh·g^{-1} after narrowing the cutoff window at 500 mA·g^{-1}, which will be higher at a low current density. A reversible capacity of 480 mAh·g^{-1} based on the total weight of C/S composite can be retained after 1,000 cycles, corresponding to a high energy density of 864 Wh·kg^{-1}. Therefore, the high capacity and exceptional cyclic stability at different cutoff windows and robust reaction kinetics render CPAPN–S a promising cathode material for high-energy LSBs.

The reaction kinetics of CPAPN–S is further studied by CV at various scan rates, electrochemical impedance spectroscopy (EIS), and galvanostatic intermittent titration technique (GITT). With elevated scan rates from 0.1 mV·s^{-1} to 1.0 mV·s^{-1} in CV (Fig. 3*A*), the redox peak current remarkably enhances and the cathodic peak shifts to a lower potential, while the anodic peak shifts to a higher potential due to the increased polarization. The linear fit of natural logarithm ln relationship of scan rate and peak current in Fig. 3*B* displays that the slopes of cathodic and anodic peaks are 0.967 and 0.868, respectively. Since the slope values are close to 1, the reaction kinetics of CPAPN–S is mainly

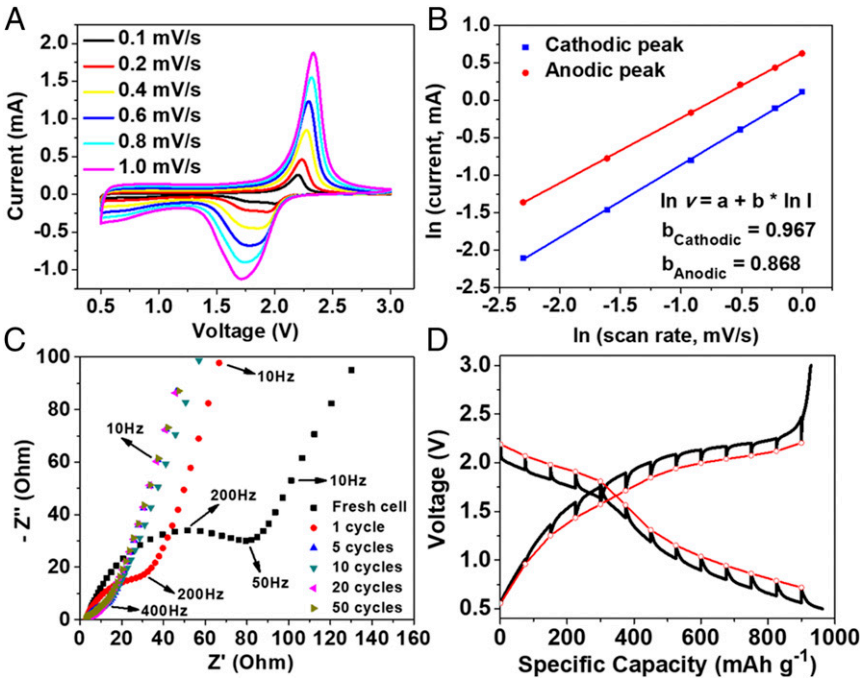

Fig. 3. Reaction kinetics of CPAPN–S. (*A*) CV of CPAPN–S at various scan rates. (*B*) The ln relationship of peak current and scan rate for CPAPN–S. (*C*) Potential response and equilibrium potential of CPAPN–S electrode during GITT measurements. (*D*) EIS analysis of CPAPN–S electrode before and after cycling.

controlled by the surface reaction (55). EIS analysis is carried out to analyze the interface resistance of the CPAPN–S electrode, which is represented by the depressed semicircle in Fig. 3*C*. The interfacial impedance of the pristine CPAPN–S electrode is ∼80 ohm, which is gradually reduced to ∼15 ohm after 50 cycles. The small interfacial impedance contributes to the fast reaction kinetics and its decrease upon cycling is probably attributed to the initial activation process, which releases more sulfur confined by the chemical bonding and enhances the reaction kinetics. GITT is conducted to further study the overpotential and equilibrium potential of CPAPN–S during initial charge and discharge cycles. As shown in Fig. 3*D*, the overpotential is ∼0.15 V, and there are two discharge equilibrium plateaus centered at 2.0 V and 0.8 V, corresponding to the lithiation of small sulfur molecules and the activation of the chemical bonding confined sulfur, respectively. The CV, EIS, and GITT results confirm the robust reaction kinetics and the initial activation process of the CPAPN–S electrode.

Since CPAPN–S exhibits excellent electrochemical performance in the FE, its electrochemical behaviors at a high carbon–sulfur loading of ∼10 $mg{\cdot}cm^{-2}$ under LEC is further investigated. The electrolyte to sulfur ratio used for the lean electrolyte LSBs is 3 mL_E/g_S. The lean electrolyte LSBs are initially tested with the commercial electrolyte (1M $LiPF_6$ in EC/DMC). The small-sulfur-based cathode undergoes a quasi-solid-state reaction mechanism during lithiation/delithiation. The small sulfur molecule and its discharged species are insoluble in the electrolytes. In addition, the discharged sulfur species in the cathode can react with the carbonate solvents in the electrolyte to generate a stable SEI (56). The SEI mainly consists of an LiF-based inorganic layer and a lithium ethylene monocarbonate/lithium methyl carbonate–based organic layer (57). The stable SEI prevents the further reaction between discharged sulfur species and solvents in the electrolyte and avoids the decomposition of organic electrolyte at low reaction potentials. The stable SEI improves the electrochemical performance of LSBs. As shown in Fig. 4*A*, the charge/discharge curves under LEC are similar to that under FE (*SI Appendix*, Fig. S8*E*), while the initial capacity (787 $mAh{\cdot}g^{-1}$/7.87 $mAh{\cdot}cm^{-2}$) under LEC is much lower than that (∼1,000 $mAh{\cdot}g^{-1}$) under FE, owing to the higher mass loading of sulfur and lesser amount of electrolyte for the LEC test. In the long-term cycling test (Fig. 4*B*), CPAPN–S undergoes fast capacity decay to 470 $mAh{\cdot}g^{-1}$ (4.7 $mAh{\cdot}cm^{-2}$) after 50 cycles, which is much worse than that under FE. As is well known, the lithium metal anode suffers from low CE in the commercial carbonate-based electrolyte due to the continuous side reaction between the organic electrolyte and lithium metal, which consumes a large amount of electrolyte during the long-term cycling. To overcome the challenge of lithium metal anode and enhance the performance of CPAPN–S under LEC, we use a 1.0 M $LiPF_6$ in FEC:FEMC:HFE all-fluorinated organic electrolyte (AFOE) for the lean electrolyte LSB test, because AFOE can suppress the lithium dendrite growth and enhance the lithium plating/stripping CE to >99.2%. As shown in Fig. 4*C*, the charge/discharge curves of CPAPN–S in AFOE are similar to that in the commercial carbonate-based electrolyte, while there is a small plateau at 1.25 V due to the formation of LiF-rich SEI on CPAPN–S from the decomposition of AFOE. The LiF-rich SEI layer also formed on Li anode, which can suppress the lithium dendrite growth. With AFOE, the CPAPN–S-based lean electrolyte LSBs display exceptional electrochemical cycling stability such that a reversible capacity of 541 $mAh{\cdot}g^{-1}$ (5.41 $mAh{\cdot}cm^{-2}$) is retained after 200 cycles (Fig. 4*D*), and the CE is close to 100%. This result proves that CPAPN–S is stable under LEC, while the key to improve the performance of lean electrolyte LSBs is to further enhance the lithium plating/striping efficiency and prevent the consumption of electrolyte by the lithium metal anode. The CE of lithium plating/striping could be further improved to 99.5% by using the other types of high-concentration fluorinated electrolyte (58). In addition, the artificial solid electrolyte interface consisting of LiF could be used to protect the lithium metal surface and prevent the lithium dendrite growth, which further improves the electrochemical performance of the lean electrolyte LSBs (53).

Discussion

The excellent cycle life of the carbon/sulfur composite in both FE and lean electrolyte is due to the formation of small sulfur molecules in the carbon matrix and the strong chemical bonding between C/O and S in the composite. The molecular-level distribution of sulfur in the carbon matrix accommodates the sulfur species upon lithiation/delithiation processes. In addition, the small sulfur and its discharged species are insoluble in the organic electrolyte. Moreover, the small-sulfur-based cathode material undergoes a quasi-solid-state reaction mechanism. The consumption of organic electrolyte is mainly attributed to the formation of solid-electrolyte interphase. As shown in the SEM and TEM images (Fig. 1 *G* and *H*), CPAPN–S consists of microsized particles, and the surface area is small, so a very small amount of electrolyte is required for the formation of SEI, and the high stability is retained in both flooded and lean electrolytes. Since CPAPN–S exhibits exceptional performance in LSBs under both FE and LEC, the reaction mechanism was explored by XPS and pair distribution function (PDF) experiments. The C 1s, N 1s, and S 2p spectra (Fig. 5 *A–C*) of the fresh (before cycling) CPAPN–S electrode is similar to CPAPN–S materials in Fig. 1 *D–F*, while a broad peak at 286.7 eV (C–O–R) and a smaller peak at 289 eV (ROC=O) in C 1s spectrum (Fig. 5*A*) are attributed to the oxidized carbon in the sodium alginate binder. CPAPN–S electrodes at different charge and discharge stages were also analyzed using XPS. When discharged to 1 V (Fig. 5*D*), the oxidized nitrogen peak in the pristine electrode (Fig. 5*B*) disappears, indicating the dissociation of the N–O bond during the lithiation. Further discharging the CPAPN–S to 0.5 V (Fig. 5*E*) results in the increased intensity ratio of the C–N–C peak to C–N=C peak, while charging CPAPN–S back to 3 V (Fig. 5*F*) leads to the decrease of the C–N–C to C–N=C peak ratio, demonstrating that during lithiation process lithium ion interacts with nitrogen in the carbon matrix and converts the C–N=C group to C–N–C group, while during the delithiation process the C–N=C group is recovered. Compared to the C–N–C peak in the pristine electrode (Fig. 5*B*), the weaker intensity after the initial cycle at 3 V (Fig. 5*F*) demonstrates the strong interaction between lithium ion and nitrogen, which changes the structure of nitrogen in the carbon matrix and stabilizes the lithium sulfides upon cycling. In the S 2p spectrum (Fig. 5*G*), the XPS peaks at 161.4 eV/162.6 eV for Li_2S_2 is generated after lithiating CPAPN–S to 1 V, while further discharging to 0.5 V (Fig. 5*H*) results in the coexistence of Li_2S_2 and Li_2S, demonstrating the step-by-step reduction process of sulfur in CPAPN–S. After delithiation to 3 V (Fig. 5*I*), the peaks for Li_2S_2 and Li_2S still exist in the cycled CPAPN–S electrode, indicating that the delithiation process of small sulfur molecules is incomplete at 3.0 V due to the large polarization at a high current rate. Moreover, XPS peaks at 169.5 eV/170.7 eV stand for the oxidized sulfur such as SO_x ($x > 2$), coming from the SEI layer, and the small peak at 167.3 eV/168.5 eV is also assigned to the oxidized sulfur in the SEI layer or inside the CPAPN–S matrix, but these peaks disappear after full discharge, forming Li_2S and Li_2O after lithiation of the oxygen-bonded sulfur. The existence of S–O in this spectrum can be identified by a combination of the imperfect fit of the Shiley background, as evidenced by the signal beneath the background and the decreased signal to noise of this spectrum compared to the others. The formation of Li_2O can be confirmed in the O 1s spectra before and after 10 min Ar sputtering. As shown in Fig. 5 *J–L*, the cycled CPAPN–S electrodes at 1 V, 0.5 V, and 3 V only show a strong peak at 532 eV for the oxygen in organic compounds due to the formation of

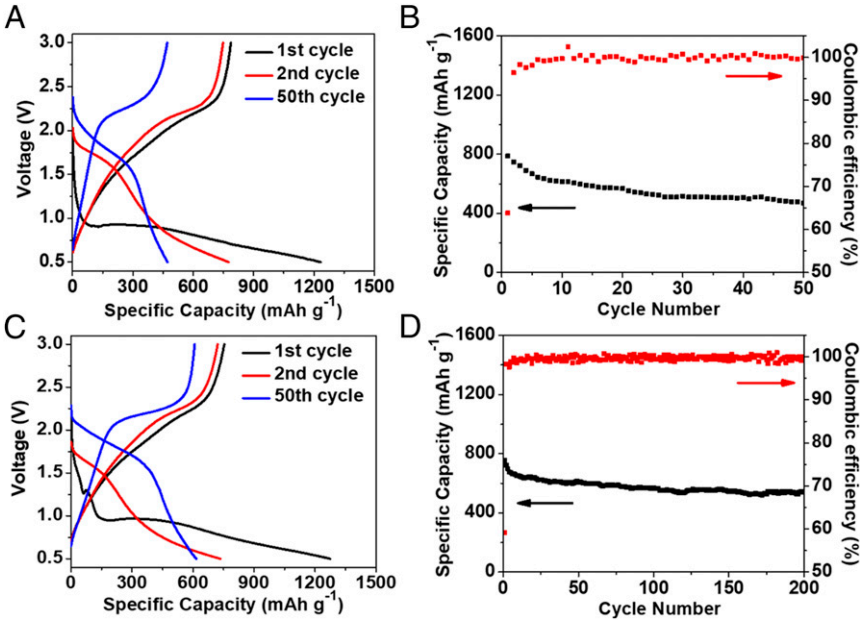

Fig. 4. Electrochemical behaviors of CPAPN–S under LEC. (*A*) The galvanostatic charge and discharge curves at 50 mA·g^{-1}/0.5 mA·cm^{-2} in commercial 1M $LiPF_6$ in EC/DMC lean electrolyte. (*B*) Delithiation capacity and CE versus cycle number in commercial 1M $LiPF_6$ in EC/DMC lean electrolyte. (*C*) The galvanostatic charge and discharge curves at 50 mA·g^{-1}/0.5 mA·cm^{-2} in all-fluorinated 1M $LiPF_6$ in FEC:FEMC:HFE lean electrolyte. (*D*) Delithiation capacity and CE versus cycle number in all-fluorinated 1M $LiPF_6$ in FEC:FEMC:HFE lean electrolyte. (Note: the specific capacity is calculated based on the total weight of C/S composite with an area mass loading of ~10 mg·cm^{-2}.)

oxidized carbon and oxidized sulfur in the organic layer of SEI, which covers the O 1s signal from the lithiated CPAPN–S sample. After 10 min of Ar sputtering, the SEI layer is removed, and the peak at 528.5 eV for Li_2O can be observed in Fig. 5 *M–O*. When discharged to 1 V (Fig. 5*M*), there is a small Li_2O peak, and it becomes much stronger after discharged to 0.5 V (Fig. 5*N*), demonstrating the dissociation of the S–O bond by Li^+ and the formation of Li_2O during the deep discharging. Then, the electrode is charged back to 3 V, and the Li_2O peak becomes weaker but still exists (Fig. 5*O*), confirming that deep discharging can break the S–O bond and generate Li_2O. The PDF analysis was adopted to analyze the activation mechanism as it is ideal for analyzing complicated structure without crystallinity requirement. PDF is basically a histogram of all of the atomic pairs whose corresponding peak intensity is weighted by the abundance of the pairs and the X-ray scattering power of involved atoms. It is therefore possible to directly monitor the evolution of bonds of interest during electrochemical cycling. Fig. 6*A* shows the PDF data of pristine sulfur and CPAPN–S. The PDF of S_8 is used as control. The puckered ring structure of S_8 is illustrated in the inset graph. It indicates that peaks 1 through 5 in sulfur PDF can be directly correlated with S–S atomic pairs within the S_8 molecule and between the molecules. Similarly, the PDF data of CPAPN–S show the presence of S–O (1.42 Å), S–C (1.76 Å), and S–S (2.07 Å) bonds in the material which are in good agreement with previous XPS studies. It is noted that the S–S bond length in CPAPN–S is very similar to that in the pure sulfur (2.06 Å, peak 1 in sulfur PDF). Fig. 6*B* shows the PDF data of ex situ CPAPN–S during the first cycle. It clearly indicates that upon lithiation the bond lengths of S–O, S–C, and S–S generally increase during discharge and decrease during charge. As illustrated by the arrows, the bond lengths generally show partially reversible change during the first cycle, suggesting the success of the proposed modification strategy by introducing the functional groups. A more detailed comparison between PDF data of the pristine material and the charged sample (Fig. 6*C*) indicates that the S–O peak intensity decreases and the S–S peak intensity increases after the first cycle. This is very likely caused by the breakage of some of the S–O bonds and more availability of the S–S bond. Interestingly, the second cycle electrochemical profile shows more capacity above 1 V, which is very likely contributed by lithium bonded to S–S parts. A schematic illustration (Fig. 6*D*) for the synthetic process of CPAPN–S is presented based on the material characterizations and XPS and PDF results. When the mixture of sulfur, PAN, and PTCDA is annealed at 600 °C, the ring-structured S_8 is vaporized and dissociated into small sulfur molecules such as S_2 and S_3, while PAN and PTCDA are carbonized to oxygen- and nitrogen-containing carbon matrix at the same time. Then, the small sulfur molecules bond with -C and -O groups in CPAPN to provide the chemical bonding-stabilized high-capacity SSCCs. The resulting SSCCs are promising cathode materials for high energy lean electrolyte LSBs.

In summary, a chemical bonding-stabilized high-capacity carbon/small sulfur composite was synthesized by carbonizing the oxygen-rich PTCDA and nitrogen-rich PAN with sulfur. The strong chemical bonding of C–S and O–S groups in the CPAPN–S composite is confirmed by the Raman spectroscopy, FTIR, XPS, and PDF characterizations. Due to the strong oxygen–sulfur and carbon–sulfur bonding, a high sulfur loading of 60 wt % with uniform distribution at a molecular level was obtained, and a high sulfur utilization of 87% with a high capacity of ~870 mAh·g^{-1} based on the total weight of CPAPN–S was achieved through a solid-state reaction between small sulfur molecules and Li-ions. The shuttle effect is completely avoided because of the absence of polysulfides in the solid-state reaction. The reversible reaction of small sulfur molecules and Li-ions during cycling and irreversible activation process of $4Li^+ + 4e^- + O–S \rightarrow Li_2O + Li_2S$ is proved by XPS and PDF. The CPAPN–S is stable for 1,000 cycles in LSBs with FE at both wide and narrow cutoff windows. More importantly, with the assistance of AFOE to stabilize the lithium metal anode, the high-capacity and stable CPAPN–S-based LSBs are also achieved under LEC, which is critical for practical application. Therefore, the chemical bonding stabilized carbon/small sulfur composite

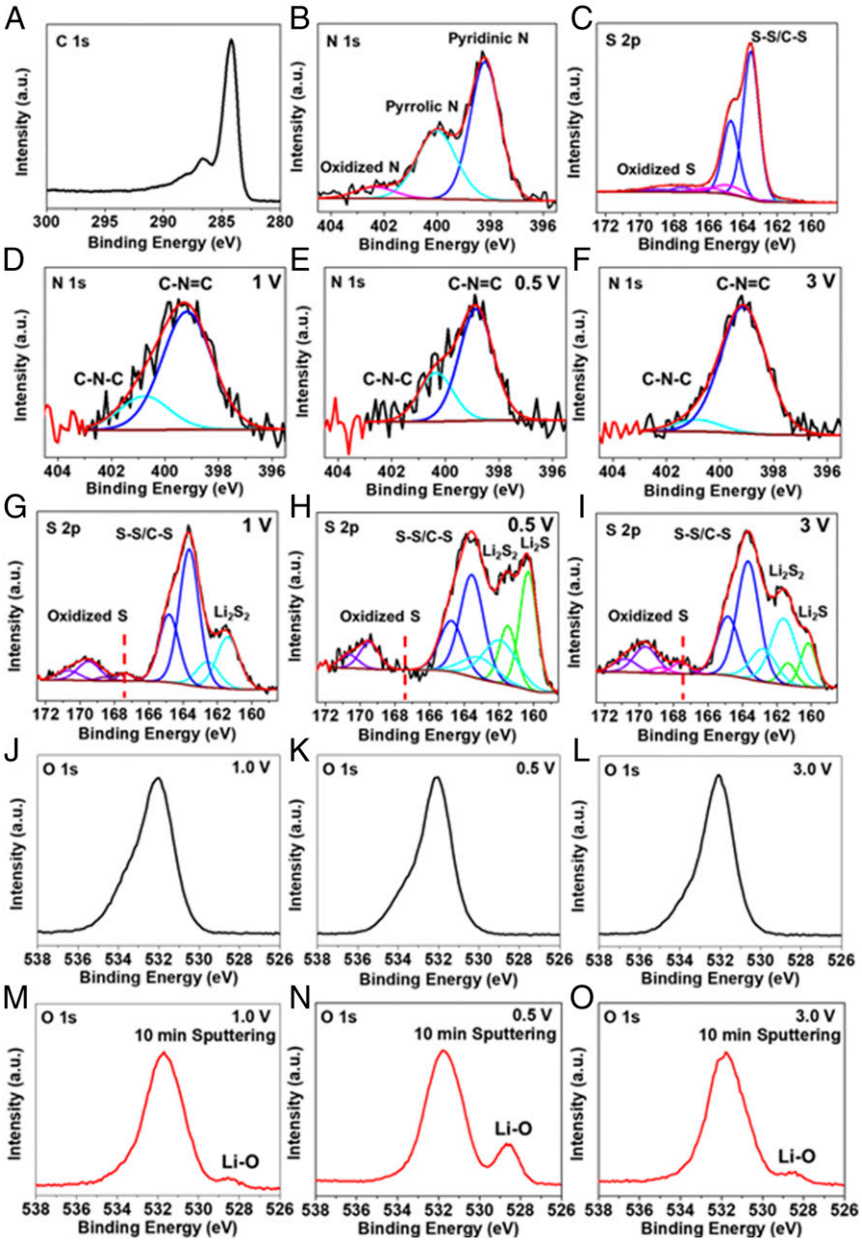

Fig. 5. XPS analysis for CPAPN–S electrode before and after cycling. XPS spectra of the pristine electrode for (*A*) C 1s, (*B*) N 1s, (*C*) S 2p; XPS spectra for N 1s after (*D*) discharged to 1 V, (*E*) discharged to 0.5 V, (*F*) charged back to 3 V; XPS spectra for S 2p after (*G*) discharged to 1 V, (*H*) discharged to 0.5 V, (*I*) charged back to 3 V; XPS spectra for *O* 1 s after (*J*) discharged to 1 V, (*K*) discharged to 0.5 V, (*L*) charged back to 3 V; XPS spectra for *O* 1 s with 10 min sputtering after (*M*) discharged to 1 V, (*N*) discharged to 0.5 V, (*O*) charged back to 3 V.

(CPAPN–S) is a promising cathode material for high-energy and long-cycle-life lean electrolyte LSBs.

Materials and Methods

Synthesis of C/S Composites. All chemicals were purchased from Sigma-Aldrich and used as received. Sulfur, perylene-3, 4, 9, 10-tetracarboxylic dianhydride, and polyacrylonitrile were mixed with a ratio of 5:1:1 by weight and sealed in a glass tube under vacuum. The sealed glass tube was annealed in an oven at 600 °C for 3 h, and it was cooled to room temperature in 24 h. The carbon–small sulfur composites were collected as black powder.

Material Characterizations. SEM images were taken by Hitachi SU-70 analytical ultrahigh-resolution SEM (Japan); TEM images were taken by JEOL (Japan) 2100F field emission TEM; TG analysis was carried out using a thermogravimetric analyzer (TA Instruments) with a heating rate of 10 °C min^{-1} in argon; XRD pattern was recorded by Bruker Smart1000 (Bruker AXS Inc.) using CuKα radiation; Raman measurements were performed on a Horiba Jobin Yvon Labram Aramis using a 532-nm diode-pumped solid-state laser, attenuated to give ∼900 μW power at the sample surface. The XPS analysis was performed on a high-sensitivity Kratos AXIS 165 X-ray photoelectron spectrometer operating in hybrid mode using monochromatic Al Kα radiation (240 W). Survey spectra and high-resolution spectra were collected with pass energies of 160 eV and 40eV, respectively. Samples were isolated from sample ground using glass slides and charge neutralization was required to minimize sample charging. Samples were loaded on the sample holder in an argon glove box; they were then sealed in two Ziploc bags and transferred into the XPS chamber in a glove bag that was purged with dry nitrogen for at least 20 min. Samples were exposed to the glove bag nitrogen environment for less than 30 s. The XPS peak fitting was done using CASA XPS with peaks shapes generated from a 30% Lorentzian/70% Gaussian product function, after application of a Shirley background. For N 1s peak fits, peaks were constrained to have equal full width at half maximum (FWHM). For the S 2p spin–orbit split pairs of peaks were constrained to have equal FWHM,

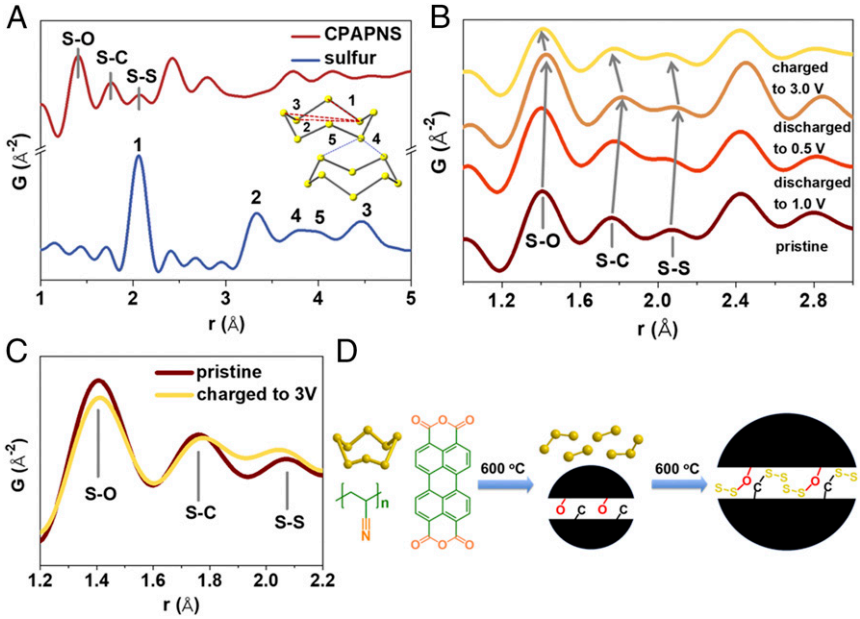

Fig. 6. PDF analysis and schematic illustration of the synthetic process of CPAPN–S. (*A*) PDF data of sulfur and CPAPN–S. Characteristic bonds and their corresponding PDF peaks are labeled. (*B*) PDF data of pristine and ex situ CPAPN–S electrodes in the first cycle, indicating that S–O, S–C, and S–S bond lengths generally increase during discharge and decrease during charge. (*C*) PDF data of charge-to-3 V electrode overlaid on the pristine data (without offset), showing the decrease of S–O peak and increase of S–S peak after first cycle. (*D*) A schematic illustration of the formation of chemical bonding stabilized carbon–small sulfur composite.

fixed area ratio of 2p 3/2:1/2 of 2:1, and spin–orbit splitting separation of 1.18 eV; furthermore, for consistent fitting the S 2p peak for S^{-1} was fixed to be 2.25 eV below the S^0 peak. The fluorine peak at 685.2 eV was used as a reference peak for the calibration of the other peaks for pristine and cycled CPAPN–S electrode. The elemental analysis was performed by ALS Environmental Company. FTIR was recorded by NEXUS 670 FT-IR instrument. PDF experiments were carried out at the X-ray Powder Diffraction beamline (28-ID-2) at the National Synchrotron Light Source II, Brookhaven National Laboratory. As the ex situ samples are air-sensitive, they were loaded into capillaries in the Ar-filled glovebox, then they were brought to the beamline and exposed to high-energy X-ray with a photon wavelength of 0.1855 Å. Considering that these samples are dominated by low scattering elements, a long time exposure (30 min) was used to ensure good statistics, especially at high *Q*. An empty capillary was also carefully measured for background subtraction. A large-area amorphous-silicon-based detector was used to collect data to high values of momentum transfer (Q_{max} = 22 $Å^{-1}$). The raw images were integrated using the software FIT2d (59). PDFgetX3 was used to correct the data for background contributions, Compton scattering and detector effects, and to Fourier-transform the data to generate $G_{(r)}$, the PDF (60):

$$G_{(r)} = 4\pi r\left[\rho_{(r)} - \rho_0\right] = \frac{2}{\pi}\int_0^\infty Q[S_{(Q)} - 1]\sin(Qr)dQ. \quad [1]$$

Here $\rho_{(r)}$ is the microscopic pair density, ρ_0 is the average number density, and Q is magnitude of the scattering vector. For elastic scattering $Q = 4\pi\sin(\theta)/\lambda$, with 2θ being the scattering angle and λ the wavelength of the radiation used. $S_{(Q)}$ is the total scattering function.

Electrochemical Measurements. The carbon–small sulfur composites were mixed with carbon black and sodium alginate binder to form a slurry at the weight ratio of 80:10:10. The electrode was prepared by casting the slurry onto aluminum foil using a doctor's blade and dried in a vacuum oven at 60 °C overnight. The slurry coated on aluminum foil was punched into circular electrodes with an area mass loading of 1.2 $mg{\cdot}cm^{-2}$. Coin cells for LSBs were assembled with lithium foil as the counterelectrode, 1M $LiPF_6$ in a mixture of ethylene carbonate/diethyl carbonate (EC/DEC, 1:1 by volume), and Celgard3501 (Celgard, LLC Corp.) as the separator. For the lean electrolyte LSBs, the carbon–small sulfur composites were mixed with carbon black and polytetrafluoroethylene binder to form a slurry at the weight ratio of 80:10:10. The stainless-steel mesh was used as the current collector, and the area mass loading of the carbon–small sulfur composites was ∼10 $mg{\cdot}cm^{-2}$. Coin cells for lean electrolyte LSBs were assembled with lithium foil as the counterelectrode, 1M lithium hexafluorophosphate ($LiPF_6$) in a mixture of fluoroethylene carbonate/3,3,3-fluoroethylmethyl carbonate/1,1,2,2-tetrafluoroethyl-2′,2′,2′-trifluoroethyl ether (FEC:FEMC:HFE, 2:6:2 by weight) as the electrolyte. The ratio of electrolyte to sulfur under LEC is ∼3 mL_E/g_S. Twofold excess lithium metal is used for the lean electrolyte LSB test. Electrochemical performance was tested using Arbin battery test station (BT2000; Arbin Instruments). Capacity was calculated on the basis of the total weight of carbon–small sulfur composites. The energy density is calculated based on the total weight of the C/S composite, using the product of the specific capacity and the average discharge potential. The average discharge potential of the CPAPN–S electrode is 1.8 V. Cyclic voltammograms were recorded using Gamry Reference 3000 Potentiostat/Galvanostat/ZRA with a scan rate of 0.1 $mV{\cdot}s^{-1}$. Impedance analysis was also performed by Gamry Reference 3000 Potentiostat/Galvanostat/ZRA. The equilibrium (open-circuit) potential of the cells is obtained by a GITT, which consists of a series of current pulses for 30 min, followed by a 6-h relaxation process. The open-circuit voltage at the end of relaxation is the thermodynamically equilibrium potential. The sulfur utilization is calculated based on the specific capacity of the CPAPN–S electrode at 50 $mA{\cdot}g^{-1}$. The first discharge capacity (around 1,250 $mAh{\cdot}g^{-1}$) was not used, because of the capacity contribution from the SEI formation and side reactions of C–S and O–S groups during the first discharge. The capacity of 870 $mAh{\cdot}g^{-1}$ based on the total weight of CPAPN–S was used for the calculation of the sulfur utilization. Since the capacity of sulfur (1,672 $mAh{\cdot}g^{-1}$) is over 18 times higher than that of the CPAPN carbon (90 $mAh{\cdot}g^{-1}$; *SI Appendix*, Fig. S9) and the mass content of sulfur (60 wt %) is twice higher than carbon (29 wt %) in the CPAPN–S composite, we ignored the capacity contribution from the CPAPN carbon. Assuming the sulfur utilization is X, and the following equation was used to calculate the sulfur utilization. (60% is the sulfur mass content in the CPAPN–S composite):

$$X \bullet 60\% \bullet 1,672\ mAh\cdot g^{-1} = 870\ mAh\cdot g^{-1}$$

$$X \approx 87\%.$$

Data Availability. All relevant data are provided as Datasets S1–S37.

ACKNOWLEDGMENTS. This work was supported by the US Department of Energy (DOE) under Awards DEEE0008202 and DEEE0008200. The support of the Maryland NanoCenter and its AIMLab is acknowledged. The work done at Brookhaven National Laboratory was supported by the Assistant Secretary for Energy Efficiency and Renewable Energy, Vehicle Technology Office of the United States through the Advanced Battery Materials Research Program, including Battery500 Consortium under Contract DE-SC0012704. This research used beamline 28-ID-2 of the National Synchrotron Light Source II, a US DOE Office of Science User Facility operated for the DOE Office of Science by Brookhaven National Laboratory under Contract DE-SC0012704.

1. D. Larcher, J.-M. Tarascon, Towards greener and more sustainable batteries for electrical energy storage. *Nat. Chem.* **7**, 19–29 (2015).
2. C. P. Grey, J. M. Tarascon, Sustainability and in situ monitoring in battery development. *Nat. Mater.* **16**, 45–56 (2016).
3. J. B. Goodenough, Y. Kim, Challenges for rechargeable Li batteries. *Chem. Mater.* **22**, 587–603 (2010).
4. B. L. Ellis, K. T. Lee, L. F. Nazar, Positive electrode materials for Li-ion and Li-batteries. *Chem. Mater.* **22**, 691–714 (2010).
5. Y. K. Sun *et al*., High-energy cathode material for long-life and safe lithium batteries. *Nat. Mater.* **8**, 320–324 (2009).
6. X. Zeng, C. Zhan, J. Lu, K. Amine, Stabilization of a high-capacity and high-power nickel-based cathode for Li-ion batteries. *Chem* **4**, 690–704 (2018).
7. F. Wu *et al*., Ultrathin spinel membrane-encapsulated layered lithium-rich cathode material for advanced Li-ion batteries. *Nano Lett.* **14**, 3550–3555 (2014).
8. M. Ben Yahia, J. Vergnet, M. Saubanère, M. L. Doublet, Unified picture of anionic redox in Li/Na-ion batteries. *Nat. Mater.* **18**, 496–502 (2019).
9. B. Kang, G. Ceder, Battery materials for ultrafast charging and discharging. *Nature* **458**, 190–193 (2009).
10. M. Winter, B. Barnett, K. Xu, Before Li ion batteries. *Chem. Rev.* **118**, 11433–11456 (2018).
11. D. Aurbach, E. Zinigrad, Y. Cohen, H. Teller, A short review of failure mechanisms of lithium metal and lithiated graphite anodes in liquid electrolyte solutions. *Solid State Ion.* **148**, 405–416 (2002).
12. X. Ji, K. T. Lee, L. F. Nazar, A highly ordered nanostructured carbon-sulphur cathode for lithium-sulphur batteries. *Nat. Mater.* **8**, 500–506 (2009).
13. P. G. Bruce, S. A. Freunberger, L. J. Hardwick, J. M. Tarascon, Li-O_2 and Li-S batteries with high energy storage. *Nat. Mater.* **11**, 19–29 (2011).
14. Y. Zhao, W. Wu, J. Li, Z. Xu, L. Guan, Encapsulating MWNTs into hollow porous carbon nanotubes: A tube-in-tube carbon nanostructure for high-performance lithium-sulfur batteries. *Adv. Mater.* **26**, 5113–5118 (2014).
15. C. Luo, Y. Zhu, Y. Wen, J. Wang, C. Wang, Carbonized polyacrylonitrile-stabilized SeS_x cathodes for long cycle life and high power density lithium ion batteries. *Adv. Funct. Mater.* **24**, 4082–4089 (2014).
16. A. Manthiram, Y. Fu, Y. S. Su, Challenges and prospects of lithium-sulfur batteries. *Acc. Chem. Res.* **46**, 1125–1134 (2013).
17. Z. Wei Seh *et al*., Sulphur-TiO_2 yolk-shell nanoarchitecture with internal void space for long-cycle lithium-sulphur batteries. *Nat. Commun.* **4**, 1331 (2013).
18. L. Suo, Y. S. Hu, H. Li, M. Armand, L. Chen, A new class of Solvent-in-Salt electrolyte for high-energy rechargeable metallic lithium batteries. *Nat. Commun.* **4**, 1481 (2013).
19. J. Schuster *et al*., Spherical ordered mesoporous carbon nanoparticles with high porosity for lithium-sulfur batteries. *Angew. Chem. Int. Ed. Engl.* **51**, 3591–3595 (2012).
20. N. Jayaprakash, J. Shen, S. S. Moganty, A. Corona, L. A. Archer, Porous hollow carbon@sulfur composites for high-power lithium-sulfur batteries. *Angew. Chem. Int. Ed. Engl.* **50**, 5904–5908 (2011).
21. S. Wei, L. Ma, K. E. Hendrickson, Z. Tu, L. A. Archer, Metal-sulfur battery cathodes based on PAN-sulfur composites. *J. Am. Chem. Soc.* **137**, 12143–12152 (2015).
22. M. Q. Zhao *et al*., Unstacked double-layer templated graphene for high-rate lithium-sulphur batteries. *Nat. Commun.* **5**, 3410 (2014).
23. L. Ji *et al*., Graphene oxide as a sulfur immobilizer in high performance lithium/sulfur cells. *J. Am. Chem. Soc.* **133**, 18522–18525 (2011).
24. J. Betz *et al*., Theoretical versus practical energy: A plea for more transparency in the energy calculation of different rechargeable battery systems. *Adv. Energy Mater.* **9**, 1803170 (2019).
25. G. Tan *et al*., Burning lithium in CS_2 for high-performing compact Li_2S–graphene nanocapsules for Li–S batteries. *Nat. Energy* **2**, 17090 (2017).
26. W. Xue *et al*., Intercalation-conversion hybrid cathodes enabling Li–S full-cell architectures with jointly superior gravimetric and volumetric energy densities. *Nat. Energy* **4**, 374–382 (2019).
27. X. Ji, S. Evers, R. Black, L. F. Nazar, Stabilizing lithium-sulphur cathodes using polysulphide reservoirs. *Nat. Commun.* **2**, 325 (2011).
28. J. Guo, Z. Yang, Y. Yu, H. D. Abruña, L. A. Archer, Lithium-sulfur battery cathode enabled by lithium-nitrile interaction. *J. Am. Chem. Soc.* **135**, 763–767 (2013).
29. J. Wang *et al*., Sulfur composite cathode materials for rechargeable lithium batteries. *Adv. Funct. Mater.* **13**, 487–492 (2003).
30. L. Yin, J. Wang, F. Lin, J. Yang, Y. Nuli, Polyacrylonitrile/graphene composite as a precursor to a sulfur-based cathode material for high-rate rechargeable Li-S batteries. *Energy Environ. Sci.* **5**, 6966–6972 (2012).
31. J. Guo, Y. Xu, C. Wang, Sulfur-impregnated disordered carbon nanotubes cathode for lithium-sulfur batteries. *Nano Lett.* **11**, 4288–4294 (2011).
32. S. Zheng *et al*., High performance C/S composite cathodes with conventional carbonate-based electrolytes in Li-S battery. *Sci. Rep.* **4**, 4842 (2014).
33. C. Nan *et al*., Durable carbon-coated Li2(S) core-shell spheres for high performance lithium/sulfur cells. *J. Am. Chem. Soc.* **136**, 4659–4663 (2014).
34. S. H. Chung, A. Manthiram, Designing lithium-sulfur cells with practically necessary parameters. *Joule* **2**, 710–724 (2018).
35. R. Elazari, G. Salitra, A. Garsuch, A. Panchenko, D. Aurbach, Sulfur-impregnated activated carbon fiber cloth as a binder-free cathode for rechargeable Li-S batteries. *Adv. Mater.* **23**, 5641–5644 (2011).
36. H. Wang *et al*., Graphene-wrapped sulfur particles as a rechargeable lithium-sulfur battery cathode material with high capacity and cycling stability. *Nano Lett.* **11**, 2644–2647 (2011).
37. J. Chen *et al*., Improving lithium-sulfur battery performance under lean electrolyte through nanoscale confinement in soft swellable gels. *Nano Lett.* **17**, 3061–3067 (2017).
38. G. Li *et al*., Stringed "tube on cube" nanohybrids as compact cathode matrix for high-loading and lean-electrolyte lithium-sulfur batteries. *Energy Environ. Sci.* **11**, 2372–2381 (2018).
39. H. Pan *et al*., Addressing passivation in lithium–sulfur battery under lean electrolyte condition. *Adv. Funct. Mater.* **28**, 1707234 (2018).
40. A. Bhargav, J. He, A. Gupta, A. Manthiram, Lithium-sulfur batteries: Attaining the critical metrics. *Joule* **4**, 285–291 (2020).
41. Y. Yin, A. A. Franco, Unraveling the operation mechanisms of lithium sulfur batteries with ultramicroporous carbons. *ACS Appl. Energy Mater.* **1**, 5816–5821 (2018).
42. C. Luo *et al*., Activation of oxygen-stabilized sulfur for Li and Na batteries. *Adv. Funct. Mater.* **26**, 745–752 (2016).
43. Y. Xu *et al*., Confined sulfur in microporous carbon renders superior cycling stability in Li/S batteries. *Adv. Funct. Mater.* **25**, 4312–4320 (2015).
44. S. Xin *et al*., Smaller sulfur molecules promise better lithium-sulfur batteries. *J. Am. Chem. Soc.* **134**, 18510–18513 (2012).
45. J. Song *et al*., Nitrogen-doped mesoporous carbon promoted chemical adsorption of sulfur and fabrication of high-areal-capacity sulfur cathode with exceptional cycling stability for lithium-sulfur batteries. *Adv. Funct. Mater.* **24**, 1243–1250 (2014).
46. J. Song *et al*., Strong lithium polysulfide chemisorption on electroactive sites of nitrogen-doped carbon composites for high-performance lithium-sulfur battery cathodes. *Angew. Chem. Int. Ed. Engl.* **54**, 4325–4329 (2015).
47. W. Zhou *et al*., Tailoring pore size of nitrogen-doped hollow carbon nanospheres for confining sulfur in lithium-sulfur batteries. *Adv. Energy Mater.* **5**, 1401752 (2015).
48. X. Fan *et al*., Non-flammable electrolyte enables Li-metal batteries with aggressive cathode chemistries. *Nat. Nanotechnol.* **13**, 715–722 (2018).
49. A. T. Ward, Raman spectroscopy of sulfur, sulfur-selenium, and sulfur-arsenic mixtures. *J. Phys. Chem.* **72**, 4133–4139 (1968).
50. P. Bazylewski, R. Divigalpitiya, G. Fanchini, In situ Raman spectroscopy distinguishes between reversible and irreversible thiol modifications in l-cysteine. *RSC Adv.* **7**, 2964–2970 (2017).
51. G. Yang *et al*., Synthesis of one-molecule-thick single-crystalline nanosheets of energetic material for high-sensitive force sensor. *Sci. Rep.* **2**, 698 (2012).
52. B. J. Lindberg *et al*., Molecular spectroscopy by means of ESCA II. Sulfur compounds. Correlation of electron binding energy with structure. *Phys. Scr.* **1**, 286–298 (1970).
53. L. Wang *et al*., Engineering of lithium-metal anodes towards a safe and stable battery. *Energy Storage Mater.* **14**, 22–48 (2018).
54. J. Chen *et al*., Electrolyte design for Li metal-free Li batteries. *Mater. Today*, 10.1016/j.mattod.2020.04.004 (2020).
55. V. Augustyn *et al*., High-rate electrochemical energy storage through Li+ intercalation pseudocapacitance. *Nat. Mater.* **12**, 518–522 (2013).
56. A. Rosenman *et al*., Facile synthesis and very stable cycling of polyvinylidene dichloride derived carbon: Sulfur composite cathode. *J. Electrochem. Soc.* **163**, A1829–A1835 (2016).
57. L. Wang *et al*., Compositions and formation mechanisms of solid-electrolyte-interphase (SEI) on microporous carbon/sulfur cathodes. *Chem. Mater.*, 10.1021/acs.chemmater.9b05027 (2020).
58. S. Chen *et al*., High-voltage lithium-metal batteries enabled by localized high-concentration electrolytes. *Adv. Mater.* **30**, e1706102 (2018).
59. A. P. Hammersley, S. O. Svensson, M. Hanfland, A. N. Fitch, D. Häusermann, Two-dimensional detector software: From real detector to idealised image or two-theta scan. *High Press. Res.* **14**, 235–248 (1996).
60. P. Juhás, T. Davis, C. L. Farrow, S. J. L. Billinge, PDFgetX3: A rapid and highly automatable program for processing powder diffraction data into total scattering pair distribution functions. *J. Appl. Cryst.* **46**, 560–566 (2013).